Density analysis based on normalized process diagrams : a comparative review of ferromagnetic alloys produced by laser powder bed fusion

Abilo Andrés Velásquez Salazar, Yuyang Li, Alejandro Ospina Vargas, Meher Zaied, Noureddine Fenineche, Jérôme Favergeon, Thierry Baffie, Salima Bouvier

Density Analysis based on Normalized Process Diagrams : A Comparative Review of Ferromagnetic Alloys Produced by Laser Powder Bed Fusion

1st Abilo Andrés Velásquez Salazar
Université de Technologie de Compiègne,
Roberval (Mechanics, energy and electricity),
Centre de recherche de Royallieu - CS 60 319 - 60 203
Compiègne Cedex - France
aavelasquezs@unal.edu.co

2nd Yuyang Li
Université de Technologie de Compiègne,
Roberval (Mechanics, energy and electricity),
Centre de recherche Royallieu - CS 60 319 - 60 203
Compiègne Cedex - France

3rd Alejandro Ospina Vargas
Université de Technologie de Compiègne,
Roberval (Mechanics, energy and electricity),
Centre de recherche Royallieu - CS 60 319 - 60 203
Compiègne Cedex - France

4th Meher Zaied
ICB LERMPS ICB UMR 6303, CNRS
Univ. Bourgogne Franche-Comté, UTBM, F-90010
Belfort, France.

5th Noureddine Fenineche
ICB LERMPS ICB UMR 6303, CNRS
Univ. Bourgogne Franche-Comté, UTBM, F-90010
Belfort, France

6th Jêrome Favergeon
Université de Technologie de Compiègne,
Roberval (Mechanics, energy and electricity),
Centre de recherche Royallieu - CS 60 319 - 60 203
Compiègne Cedex - France

7th Thierry Baffie
CEA, LITEN,
Université Grenoble Alpes,
Grenoble, France

8th Salima Bouvier
Université de Technologie de Compiègne,
Roberval (Mechanics, energy and electricity),
Centre de recherche Royallieu - CS 60 319 - 60 203
Compiègne Cedex - France

2024 International Conference on Electrical Machines (ICEM) | 979-8-3503-7060-7/24/$31.00 ©2024 IEEE | DOI: 10.1109/ICEM60801.2024.10700463

***Abstract*—This research explores additive manufacturing of magnetic materials via Selective Laser Melting (SLM), integrating insights from prior studies. Emphasizing density variation concerning applied energies, our methodology incorporates normalized process diagrams. This analysis revealing an identification of different density regions in the case of Fe-6.5%wt. Si alloy. These regions show the interplay between process parameters and thermophysical material properties, encompassing lack of fusion, keyhole pores and balling. Further, density variations of Fe-3% wt. Si, Fe-6.7%wt. Si, and Fe-6.9%wt. Si alloys are studied, highlighting the impact of silicon content on final density. The present study contributes to understand dynamic interactions shaping magnetic material density. By optimizing process parameters based on density considerations, microstructure tailoring becomes possible, and, so far, an optimization of the magnetic properties.**

The authors acknowledge the financial support of the Hauts- de-france region in the frame of the " CONTRAT PLAN ÉTAT-RÉGION 2021-2027 EE 4.0" as well as the French National Research Agency (ANR) through the FALSTAFF project N° ANR-22-CE08-0029-01. The authors are also grateful to Roberval-UTC and ICB-LERMPS technical staff for their support.

***Index Terms*—Additive Manufacturing, Selective Laser Melting (SLM), Normalized diagrams, Magnetic Materials**

I. Introduction

For more than a century, FeSi alloys have been used in the laminated cores of electric machines [1] [2], there are numerous studies on the physical and mechanical properties of these alloys, their production methods, and composition. Nevertheless, the use of additive manufacturing (AM) as an alternative method to produce electric machines prototypes introduce new questions about the optimization of magnetics parts properties. AM can be defined as a manufacturing process based on digital models, involving a layer-by-layer construction of objects, specifically the Laser Powder Bed Fusion (LPBF) technique, which use a laser to selectively melt powders, proves to be well adapted to produce metallic parts in complex geometrical configurations, non affordable by classical productions methods (for example, lamination).

Thus, understanding and controlling the final properties of additively manufactured magnetic materials using LPBF is a critical factor for use this technology as an accelerator in the study of more energy-efficient electrical machines [3], [4].

The most important parameters in the design of electrical machinery are the magnetic saturation B_s, the coercivity H_c and the iron losses. B_s are related to the power density of electrical machines, H_c give an indication of the magnetic field H necessary to generate a desired magnetic flux density B then, indirectly, it is related to the size of windings. Finally, the iron losses represented a key factor in the design of electrical machines because they are an important parameter to determine machine efficiency and heat dissipation.

As shown by Zaied [5], B_s strongly depends of material density and can be correlated with process parameters, principally, laser power and scan velocity. Meanwhile, H_c is strongly related with material microstructure. Thus, attaining control over density and microstructure is a pivotal way for the production of magnetic materials and so far for the design of more high-efficiency electrical machines.

The main goal of this article is determine a methodology to compare different LPBF process parameters applied to the manufacturing of magnetic materials, principally, FeSi alloys with a silicium content by weight between 3% - 6%. Firstly, in section §II, a dimensional method is used, named Normalised Process Diagrams (NPD), to address a comparison, between different authors sources, concerning density variation linked to LPBF process parameters. By exploring the construction of NPD, this study adapts the non-linear behavior of density as a function of applied energies using a new consideration about the normalization quantity. Secondly, in section §III, a results analysis and discussion is conducted to understand the influence of LPBF process parameters over density and the determination of an optimum interval that produce magnetic parts with high densities. Finally, in section §IV, this article emphasizes the usefulness of NPD to the visualization of the relationship between production parameters and resulting densities under different energy levels. Thus, NPD can be a promising data analysis resource for identifying configurations that lead to density maxima. Although LPBF is not yet standardized, welding processes are, and this research effort aims to contribute to the standardization basis. Currently, we use the melt pool shape derived from an analytical solution, but we aim to incorporate the Gaussian distribution of laser energy and account for phenomena beyond conduction. This will provide increasingly accurate tools to achieve better material densities, especially for those with well-known thermal properties and laser interaction characteristics.

II. Normalised Process Diagrams (NPD)

Additive manufacturing by LPBF is a complex process that involves many variables, principally related to powder characteristics (particle size distribution, laser absorptivity, flowability, etc) and machine parameters (laser power, scan velocity, scan strategy, powder spreading, build platform temperature, etc). Different approaches can be used to simplify the analysis based on physical criteria [6], [7]. Through these approaches, the use of dimensional quantities by identification of process variables groups can simplify the physical problem and find relations between process parameters and final physical properties. Dimensional variables facilitate different comparisons and analyses across systems or experiments by eliminating the influence of absolute magnitudes. This approach enhances understanding and aids in the identification of optimal conditions.

In the context of laser processing Ion *et. al.* [8] introduce this kind of diagram to optimize laser material process, especially, laser welding. Subsequently, Thomas *et. al.* [9] adapted Ion's approach to compare and analyze different additive manufacturing technologies. Particularly, Thomas *et. al.* use the normalized process diagrams to provide a solid foundation in the pursuit of a more deeply understanding between process parameters and microstructure from different additive manufacturing technologies . Recently, Zaied *et. al.* [5] adapted this approach to analyze the relations between LPBF process parameters and magnetic properties in the case of Fe6.5% wt. Si alloy.

A. Construction of Normalized Process Maps

The process begins with the consideration of normalized volumetric energy (1), expressed as:

$$E^* = \frac{P^*}{v^* h^* l^*}, \tag{1}$$

where, the symbol * indicates that they are dimensionless parameters. These dimensionless quantities are defined as :

- P^* dimensionless laser power

$$P^* = \frac{AP}{r_b \lambda \Delta T} \tag{2}$$

  with A as the powder absorptivity, r_b the radius of the laser beam, λ the thermal conductivity, and $\Delta T = T_m - T_0$ as the difference between the melting temperature, T_m, and the initial platform temperature, T_0.
- v^* dimensionless scanning velocity

$$v^* = v r_b / \alpha, \tag{3}$$

  with v as the scanning velocity, and $\alpha = \lambda/(\rho c_p)$ as the thermal diffusivity, defined as the ratio between thermal conductivity λ and the product of density ρ and specific heat c_p.
- h^* dimensionless hatch distance

$$h^* = h / r_b. \tag{4}$$

- l^* dimensionless bed powder thickness

$$l^* = l/(2r_b). \tag{5}$$

  The units used for calculate these quantities are in the MKS system.

As proposed by Thomas *et. al.* [9] a normalised diagram is constructed where the abscissa is $P^*/(v^* l^*)$ and the ordinate $1/h^*$. Thus, the product between abscissa and ordinate is the

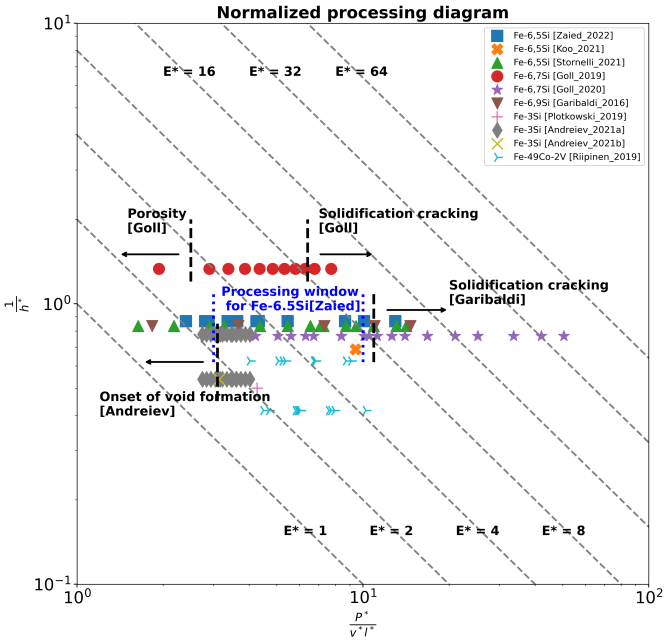

Fig. 1. Standardized process diagram of soft magnetic materials.

normalized volumetric energy (Eq. (1)). In the subsequent analysis, the normalized diagram (Fig. 1) is applied to make a review and comparison of different magnetic materials produced by LPBF, the summary of process parameters are presented in Table I and completed with tables II and III.

The positioning of data points suggest that the hatch distance ($1/h^* \approx 1$) is close to the laser spot radius. This diagram shown the effects of modifying parameters by increasing or decreasing the normalized energy and can be used to compare different manufacturing parameters. Thus, this diagram captures the occurrence of solidification cracking and porosity regions, providing valuable insights into the impact of construction parameters on mechanical properties of the material.

This approach can be very useful when comparing different materials under the same process conditions or the same material under varying conditions. Such visualizations aid in identifying trends and outliers, guiding the selection of optimal parameters for achieving desired material properties.

The tables I, II and III present comprehensive sources for both process parameter data and thermodynamic material data. The process parameter data table includes information on laser power, scanning velocity, hatch distance, and layer thickness, while the thermodynamic material data table encompasses key properties required for the additive manufacturing of magnetic materials.

In the subsequent sections, we delve into the specifics of our methodology and present our findings in the context of additive manufacturing of magnetic materials via LPBF.

A new consideration about normalized parameters

A modification suggested by Moda *et al.* [22] was adopted to obtain a more comprehensive relation between density and process parameters. The normalization quantity, defined as the laser radius, r_b, will be replaced by the estimated width of the melt pool, denoted as $2R$. This adjustment is justified because the melt pool geometry is directly related to cracking or porosity. This geometry depends not only on the laser radius but also on the thermal properties of the material and the other LPBF manufacturing parameters mentioned earlier. Moda utilizes the Rosenthal equation, solved by Mendez *et. al.* [23], to estimate the melt pool shape and thus understand the energy distribution delivered by the laser along its path. This approach highlights that an important parameter, beyond the laser spot radius r_b, is the width of the melt pool.

The Rosenthal model is used to calculate the geometry of the melt pool. This model only takes into account the heat conduction, not the convecton and the fluid dynamics in the melt pool. Thus, transverse sections of the melt pool are only hemi-spherical. Rosenthal model is well suited for predicitng width and depth in the conduction mode but not in the keyhole mode. For simplicity, we will describe only the basic calculations needed for make these changes, first the Rykalin number :

$$R_y = \frac{Pv}{4\pi\lambda\alpha\Delta T_m}, \tag{6}$$

secondly, the characteristic length :

$$l_{R_y} = \frac{2\alpha}{v}, \tag{7}$$

and finally, the half-width and depth of the melted zone is defined by :

$$R \approx l_{R_y} R_y \left[1 + \left(\frac{2}{eR_y}\right)^{\frac{\beta}{2}}\right]^{\frac{1}{\beta}}, \tag{8}$$

with $\beta = -1.7312$ which is an approximate parameter in the analytical solution.

The change in the normalization approach, between a fixed and a variable quantity, the laser spot and the size of the melt pool respectively, contribute to a better representation of the influence of process parameters, such as energy, power, scanning velocity, hatch distance, and layer thickness. This change becomes crucial in the identification of different density regions such as pore generation, partial melting regions and keyhole production. Additionally, due to the diverse nature of materials and the varying energy requirements, it can be easily adapt to different types of thermophysical properties and process parameters.

A new graph was constructed, fig. 2, applying the new consideration of the half-width of the melt pool, R, calculated by the Rosenthal equation for a point laser source, instead of the laser spot radius. This new graph shows the data points more dispersed and better reflects the energy distribution delivered to the material. Both graphs use normalized absorbed energy density. In this second graph, the same labels from the previous graph cannot be applied due to the redistribution of points. This redistribution is caused by the energy delivered creating different molten volumes, which depend on the material's

TABLE I
SUMMARY OF ADDITIVE MANUFACTURING PROCESS PARAMETERS FOR SOFT MAGNETIC MATERIALS PRESENTED IN THE LITERATURE

Article	**Alloy**	$P[W]$	$v[m.s^{-1}]$	$h[\mu m]$	$l[\mu m]$	$r_b[\mu m]$	$T_0[°C]$
Zaied 2022 [5]	Fe-6,5Si	60-90	0.15-0.5	60	30	52	240
Koo 2021 [10]	Fe-6,5Si	90	0.2	80	25	55	23
Stornelli 2021 [11]	Fe-6,5Si	75-325	0.5 - 1	60	30	50	200
Goll 2019 [12]	Fe-6,7Si	100-400	0.5	60	50	80	400
Goll 2020 [13]	Fe-6,7Si	100-300	0.1 - 0.5	60	50	46	400
Garibaldi 2016 [14]	Fe-6,9Si	70	0.125 - 1	60	25	/	200
Garibaldi 2018a [15]	Fe-6,9Si	70	0.125 - 0.5	60	25	/	200
Garibaldi 2018b [16]	Fe-6,9Si	70	0.5	60	25	/	200
Plotkowski 2019 [17]	Fe-3Si	200	0.6818	100	50	/	/
Andreiev 2021a [18]	Fe-3Si	220-280	0.65 - 0.75	90 - 130	50	70	200
Andreiev 2021b [19]	Fe-3Si	235	0.7	130	50	70	200
Riipinen 2019 [20]	Fe-49Co-2V	150-225	0.575 - 0.975	80 - 120	25	/	200

TABLE II
THERMO-PHYSICAL PROPERTIES OF FE-SI MATERIAL

Property	**Quantity**	**Unity**	**References**
Solidification temperature	1700	K	[21]
Liquefaction temperature	1773	K	[21]
Theoretical density (ρ)	7.5	g/cm^3	
Thermal conductivity (λ)	45	$W.m^{-1}.K^{-1}$	[17]
Thermal capacity of the material (c_p)	470	$J/kg.K$	[17]

TABLE III
THERMO-PHYSICAL PROPERTIES OF FE-49CO-2V WT(%) MATERIAL

Property	**Quantity**	**Unity**	**References**
Solidification temperature	1721.55	K	JMatPro
Liquefaction temperature	1733.99	K	JMatPro
Theoretical density (ρ)	$8.28(25°C)$	g/cm^3	JMatPro
Thermal conductivity (λ)	$20.85(25°C)$	$W.m^{-1}.K^{-1}$	JMatPro
Thermal capacity of the material (c_p)	$490(25°C)$	$J/kg.K$	JMatPro

new diag witjout density/fig new diag without density.png

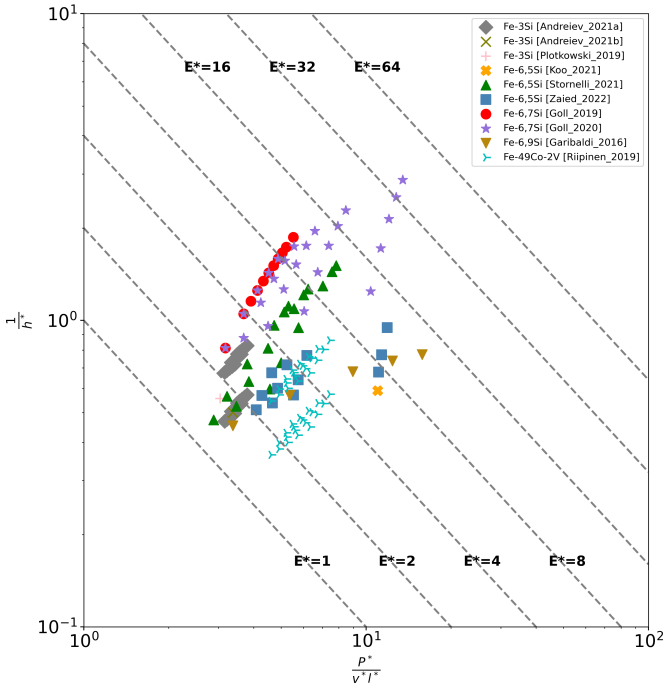

Fig. 2. Alterative standardized process diagram without density consideration of soft magnetic materials.

thermal properties and the supplied power, beyond just the laser spot radius.

III. RESULTS AND DISCUSSION

A. Density Variation in Fe-Si Alloys

In our investigation of the Fe-6.5%Si, Fe-6.7%Si, and Fe-6.9%Si alloys, data from the authors [5], [10], [11], [24], [12], and [14] were analyzed. The fig. 3 illustrates the relative density variation with respect to key process parameters, providing a comprehensive view of how different conditions influence the final density. It's important to note that this figure is scaled to the width of the melt pool, calculated using the method proposed by Mendez *et al.* and reported by Moda *et al.* on LPBF. Mendez method, derived from the Rosenthal function, defines the shape of the melt pool based on the region where the temperature is greater than or equal to the alloy's liquefaction temperature. For the aforementioned reason, this new diagram disperses information more effectively, being more sensitive to the thermal properties of the material and its density. Therefore, it is necessary to narrow the visualization window to better appreciate how these diagrams are segmented.

In the normalized energy diagram, fig. 3, it is expected that at least four distinct regions will appear, each influencing the density and providing valuable insights into the additive manufacturing process using the melt pool width for normalization. These regions are:

- **High h^* region:** At the bottom of the diagram, where the normalized hatch distance $h^* = h/R$ is relatively large ($1/h^* \to 0$), there is insufficient material melting, leading to a reduction in density. This region is characterized by

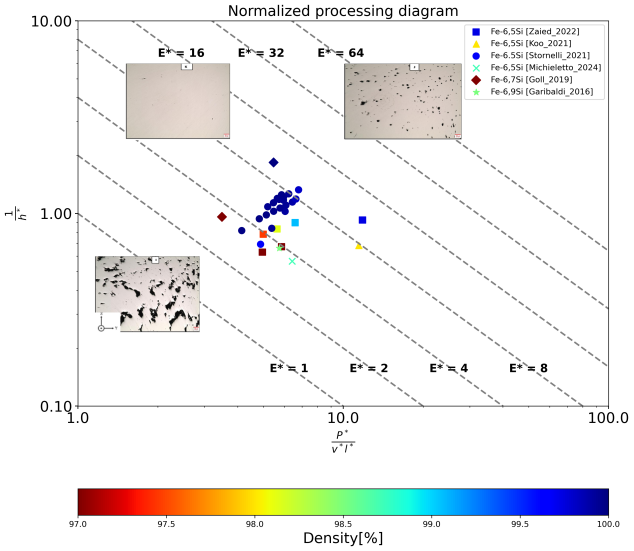

Fig. 3. Standardized process diagram for Fe-6.5Si. The micrographs were taken on the highlighted samples and represent the causes of the relative density decrease. The color on the marker represent relative density with respect to the theoretical bulk material.

a lack of fusion due to the significant spacing between scan paths. As observed in the figure, there is a noticeable decrease in density, possibly caused by this lack of fusion.

- **High energy region:** At high energy levels, normalized energy isopleths (dashed lines) between $E_0^* = [8, 16]$, small pores of evaporated material are formed. At these energies, the generation of evaporated material contributes to pore formation, causing a reduction in density. As observed in the SEM image on the right within the figure, small pores are visible, and there is a slight decrease in density, which may indicate the onset of porosity due to metal evaporation caused by the intense radiation.
- **Low energy region:** The left upper corner of the graph represents scenarios where the hatch distance is sufficiently small to melt the entire material, but the laser power is too low or the scan speed is too high, resulting in insufficient volumetric normalized energy for complete melting. This lack of sufficient energy leads to the reappearance of lack of fusion. This could be the reason for the low density observed in the data from Goll et al., even though $h^* = 1$, indicating that the separation distance between paths is equal to half the width of the melt pool.
- **High density region:** The intermediate region, situated between the extremes of energy and just above $h^* \approx 1$, represents optimal conditions where the density is close to that of solid material without pores and or lack of fusion zones. This region is characterized by a balanced combination between energy and hatch distance, resulting in an optimal density.

It's essential to note that the accuracy of these regions would be further pronounced with more precise measurements of absorptivity, thermal conductivity, heat capacity, and density. Absorptivity is a fundamental concept in these diagrams, as it significantly influences the energy absorbed by the material. As stated by Stornelli, an increase in laser energy can generate a phenomenon known as keyhole, which significantly increases the absorptivity of the incident radiation. This, in turn, raises the energy absorbed by the material, altering the dimensions and shape of the melt pool. This phenomenon is expected in the upper right part of the normalization diagram and is typically accompanied by a decrease in density due to the formation of porosities from evaporation.

In our study, we only worked with data expected to be in the conduction energy region, according to Stornelli, based on the absorptivity values reported by the authors. It is clear that absorptivity plays a crucial role in normalization diagrams. Additionally, the isolated points in the diagram may be attributed to the Gaussian distribution of power in the laser spot, a consideration not accounted for here. The Rosenthal model assumes the laser beam is a point energy source. Nevertheless, the laser spot has a Gaussian power distribution. Thus, further refinement and experimentation, considering the Gaussian laser power distribution and precise material properties, would enhance the predictive capabilities of such diagrams. This analysis underscores the intricate interplay of process parameters and their impact on the final density of the Fe-Si alloys.

IV. Conclusions and Perspectives

In conclusion, this study achieved several key outcomes. First, an enhanced normalized diagram was adapted to discern the impact of constructive parameters on the density of iron-silicon magnetic alloys. Second, density regions were identified, facilitating the targeting of optimal construction points. Third, the construction of standardized diagrams is improved by considering the shape of the melt pool rather than solely relying on the laser spot radius.

These findings contribute to a nuanced understanding of the intricate relationship between process parameters and the density of magnetic materials. The adapted normalized diagram provides valuable insights into the regions where lack of fusion caused by scanning strategy (large h), pore formation by high energy absorpted, insufficient power for material melting, and optimal conditions occur. Utilizing this information allows for a more refined optimization of process parameters, influencing microstructure and, consequently, enhancing the magnetic properties of electric steels.

This work aims to establish a comprehensive connection between density, microstructure, and magnetic properties, particularly focusing on their implications for electric machines. In the final paper, this study intends elucidate how material density and microstructural features influence magnetic behavior in the context of electric machines. By uncovering these intricate relationships, we anticipate advancing the design and optimization of magnetic materials specifically tailored for electric machine applications. This deeper understanding

holds the potential to enhance the efficiency, performance, and reliability of electric machines in various industrial and commercial settings.

REFERENCES

[1] Andreas Krings, Aldo Boglietti, Andrea Cavagnino, and Steve Sprague. Soft magnetic material status and trends in electric machines. *IEEE Transactions on Industrial Electronics*, 64(3):2405–2414, March 2017.

[2] Andreas Krings, Marco Cossale, Alberto Tenconi, Juliette Soulard, Andrea Cavagnino, and Aldo Boglietti. Magnetic materials used in electrical machines: A comparison and selection guide for early machine design. *IEEE Industry Applications Magazine*, 23(6):21–28, November 2017.

[3] T.N. Lamichhane, L. Sethuraman, A. Dalagan, H. Wang, J. Keller, and M.P. Paranthaman. Additive manufacturing of soft magnets for electrical machines—a review. *Materials Today Physics*, 15:100255, December 2020.

[4] Bryan Ramiro Rodriguez-Vargas, Giulia Stornelli, Paolo Folgarait, Maria Rita Ridolfi, Argelia Fabiola Miranda Pérez, and Andrea Di Schino. Recent advances in additive manufacturing of soft magnetic materials: A review. *Materials*, 16(16), 2023.

[5] Meher Zaied, Alejandro Ospina-Vargas, Nicolas Buiron, Jérôme Favergeon, and Nour-Eddine Fenineche. Additive manufacturing of soft ferromagnetic fe 6.5%si annular cores: Process parameters, microstructure, and magnetic properties. *IEEE Transactions on Magnetics*, 58(11):1–9, 2022.

[6] Liping Guo, Hanjie Liu, Hongze Wang, Qianglong Wei, Jiahui Zhang, Yingyan Chen, Chu Lun Alex Leung, Qing Lian, Yi Wu, Yu Zou, and Haowei Wang. A high-fidelity comprehensive framework for the additive manufacturing printability assessment. *Journal of Manufacturing Processes*, 105:219–231, 2023.

[7] Luke Johnson, Mohamad Mahmoudi, Bing Zhang, Raiyan Seede, Xueqin Huang, Janine T. Maier, Hans J. Maier, Ibrahim Karaman, Alaa Elwany, and Raymundo Arróyave. Assessing printability maps in additive manufacturing of metal alloys. *Acta Materialia*, 176:199–210, 2019.

[8] J.C. Ion, H.R. Shercliff, and M.F. Ashby. Diagrams for laser materials processing. *Acta Metallurgica et Materialia*, 40(7):1539–1551, July 1992.

[9] Meurig Thomas, Gavin J. Baxter, and Ian Todd. Normalised model-based processing diagrams for additive layer manufacture of engineering alloys. *Acta Materialia*, 108:26–35, April 2016.

[10] Bonuk Koo, Min-Sun Jang, Yeong Gyun Nam, Sangsun Yang, Jihun Yu, Yong Ho Park, and Jae Won Jeong. Structurally-layered soft magnetic fe-si components with surface insulation prepared by shell-shaping selective laser melting. *Applied Surface Science*, 553:149510, July 2021.

[11] Giulia Stornelli, Antonio Faba, Andrea Di Schino, Paolo Folgarait, Maria Rita Ridolfi, Ermanno Cardelli, and Roberto Montanari. Properties of additively manufactured electric steel powder cores with increased si content. *Materials*, 14(6):1489, March 2021.

[12] D. Goll, D. Schuller, G. Martinek, T. Kunert, J. Schurr, C. Sinz, T. Schubert, T. Bernthaler, H. Riegel, and G. Schneider. Additive manufacturing of soft magnetic materials and components. *Additive Manufacturing*, 27:428–439, May 2019.

[13] D. Goll, J. Schurr, F. Trauter, J. Schanz, T. Bernthaler, H. Riegel, and G. Schneider. Additive manufacturing of soft and hard magnetic materials. *Procedia CIRP*, 94:248–253, 2020. 11th CIRP Conference on Photonic Technologies [LANE 2020].

[14] Michele Garibaldi, Ian Ashcroft, Marco Simonelli, and Richard Hague. Metallurgy of high-silicon steel parts produced using selective laser melting. *Acta Materialia*, 110:207–216, May 2016.

[15] M. Garibaldi, I. Ashcroft, N. Hillier, S.A.C. Harmon, and R. Hague. Relationship between laser energy input, microstructures and magnetic properties of selective laser melted fe-6.9 *Materials Characterization*, 143:144–151, September 2018. Metal Additive Manufacturing: Microstructures and Properties.

[16] M. Garibaldi, I. Ashcroft, J.N. Lemke, M. Simonelli, and R. Hague. Effect of annealing on the microstructure and magnetic properties of soft magnetic fe-si produced via laser additive manufacturing. *Scripta Materialia*, 142:121–125, 2018.

[17] A. Plotkowski, J. Pries, F. List, P. Nandwana, B. Stump, K. Carver, and R.R. Dehoff. Influence of scan pattern and geometry on the microstructure and soft-magnetic performance of additively manufactured fe-si. *Additive Manufacturing*, 29:100781, October 2019.

[18] Anatolii Andreiev, Kay-Peter Hoyer, Dimitri Dula, Florian Hengsbach, Olexandr Grydin, Yaroslav Frolov, and Mirko Schaper. Laser beam melting of functionally graded materials with application-adapted tailoring of magnetic and mechanical performance. *Materials Science and Engineering: A*, 822:141662, August 2021.

[19] Anatolii Andreiev, Kay-Peter Hoyer, Dimitri Dula, Florian Hengsbach, Michael Haase, Jan Gierse, Detmar Zimmer, Thomas Tröster, and Mirko Schaper. Soft-magnetic behavior of laser beam melted fesi3 alloy with graded cross-section. *Journal of Materials Processing Technology*, 296:117183, October 2021.

[20] Tuomas Riipinen, Tomi Lindroos, Sini Metsä-Kortelainen, Janne Keränen, Juha Lagerbom, Aino Manninen, and Jenni Pippuri-Mäkeläinen. Mechanical and magnetic properties of fe-co-v alloy produced by selective laser melting. (Ltd,), 2018.

[21] Jyrki Miettinen. Calculation of solidification-related thermophysical properties for steels. *Metallurgical and Materials Transactions B*, 28(2):281–297, April 1997.

[22] Mattia Moda, Andrea Chiocca, Giuseppe Macoretta, Bernardo Monelli, and Leonardo Bertini. Technological implications of the rosenthal solution for a moving point heat source in steady state on a semi-infinite solid. *Materials & Design*, 223:110991, 07 2022.

[23] Patricio F. Mendez, Yi Lu, and Ying Wang. Scaling analysis of a moving point heat source in steady-state on a semi-infinite solid. *Journal of Heat Transfer*, 140(8), April 2018.

[24] Daniele Michieletto, Luigi Alberti, Filippo Zanini, and Simone Carmignato. Electromagnetic characterization of silicon–iron additively manufactured cores for electric machines. *Energies*, 17(3):650, January 2024.